Dy-based single-molecule magnet as a case study for magnetization relaxation under applied pressure

S. Chicco,[1] E. Garlatti,[1,2,3] A. Mavromagoulos,[4] A. B. Canaj,[4] P. Bonfà,[1] A. Piovano,[5] S. Dey,[6] H. Little,[7] A. Chiesa,[1,2,3] A. S. Ivanov,[5] I. J. Onuorah,[1] S. Parsons,[7] G. Rajaraman,[6] T. Guidi,[8,9] M. Murrie,[4,*] and S. Carretta[1,2,3,†]

[1]*Department of Mathematical, Physical and Computer Sciences, University of Parma, Parco Area delle Scienze 7/A, 43124 Parma, Italy*
[2]*INFN Sezione di Milano-Bicocca, Gruppo Collegato di Parma, 43124 Parma, Italy*
[3]*Consorzio Interuniversitario Nazionale per la Scienza e Tecnologia dei Materiali (INSTM), UdR Parma, I-43124 Parma, Italy*
[4]*School of Chemistry, University of Glasgow, Glasgow G12 8QQ, United Kingdom*
[5]*Institut Laue-Langevin (ILL), 71 Avenue des Martyrs, Grenoble, France*
[6]*Department of Chemistry, Indian Institute of Technology Bombay, Powai, Mumbai 400076, India*
[7]*EaStCHEM School of Chemistry, University of Edinburgh, EH9 3FJ Edinburgh, United Kingdom*
[8]*School of Science and Technology, Physics Division, University of Camerino, I-62032 Camerino, Italy*
[9]*ISIS Facility, Rutherford Appleton Laboratory, Didcot OX11 0QX Didcot, United Kingdom*

(Received 22 May 2025; accepted 15 December 2025; published 20 January 2026)

Molecular nanomagnets have garnered significant attention in recent years thanks to their unique potential in quantum information processing as molecular qudits and in high-density memory encoding as single-molecule magnets. However, fully unlocking the potential of these systems requires a comprehensive understanding of the interplay between the various mechanisms that govern their relaxation dynamics, which remains a noncompletely understood phenomenon. In this work, we employ a cost-effective semi-*ab initio* approach to model the magnetization relaxation dynamics in a testbed Dy-based single-molecule magnet and determine the effects of applied external pressure on the interplay between various mechanisms, such as coupling with molecular vibrations and quantum tunneling. *Ab initio* phonon calculations are validated by direct comparison with inelastic neutron scattering experiments, which are used for the first time to investigate pressure-induced modifications of phonons and vibrations in a molecular nanomagnet. The combination of our theoretical approach with different experimental techniques allows us to predict an overall acceleration of the relaxation dynamics under pressure, disentangling the role of different ingredients, such as crystal field axiality and phonons.

DOI: 10.1103/y7kz-8f3s

I. INTRODUCTION

Despite decades of investigation, the relaxation dynamics of molecular nanomagnets (MNMs), molecules containing one or few interacting paramagnetic ions, is still not completely understood. However, given that these systems have the potential to significantly impact emerging technologies, a thorough understanding of the various relaxation mechanisms would provide a crucial advantage, ultimately leading to an enhancement of the performance of these platforms.

Some MNMs, called single-molecule magnets (SMMs), display a bistable magnetic behavior [1,2] of single-molecule origin and a robust magnetic hysteresis even above liquid nitrogen temperatures (∼80 K), [3–7]. Hence, they represent promising candidates for an ultimate downscale of classical memory devices, envisaging the possibility to encode a bit of information in a nanoscale object [8,9]. In addition, MNMs are attracting increasing interest for encoding qubits or qudits, the basic units of quantum technologies [10–12]. Indeed, the energy structure of these systems, often composed of many accessible levels, was demonstrated to be efficient for storing and processing quantum information [11,13–15]. Thus, it is crucial to investigate the key factors governing the magnetization dynamics in MNMs and to disentangle their roles across different temperature regimes.

Lanthanide(Ln)-based complexes are now the prototype of SMMs and their relaxation dynamics is the result of a complex interplay between different mechanisms, whose relative importance varies with temperature and depends on the molecular structure of the system and on its phonon and vibrational spectrum [5,16–21]. On one hand, the axiality of the crystal field (CF) Hamiltonian is one of the key ingredients for limiting the efficiency of the quantum tunneling of the magnetization (QTM), which dominates relaxation at very low temperatures. On the other hand, the coupling of spins to vibrational degrees of freedom induces modulation of the anisotropy terms of the spin-Hamiltonian,

*Contact author: mark.murrie@glasgow.ac.uk
†Contact author: stefano.carretta@unipr.it

triggering phonon-assisted mechanisms like Raman or Orbach processes, also influenced by the CF eigenstates and levels [5].

All of the ingredients mentioned above, responsible for the unique behavior of MNMs, can be influenced by the application of an external hydrostatic pressure [22]. Thus, performing investigations of MNMs in applied pressure can represent an effective strategy to gain insight into the relaxation mechanisms of Ln-based systems, as an alternative to chemical/structural modifications of the molecules. Indeed, not only can applied pressure change the molecular structure and hence tune magnetic anisotropy, as shown for instance in Mn_{12} [23], and the efficiency of magnetization quantum tunneling processes, as shown in pseudo-D_{5h} symmetric Dy/Ho(III) [24], but it can also modify molecular and lattice vibrations, as proposed in Ref. [22] for a dysprosocenium complex. In this sense, pressure is a unique tool that was often used to modulate the phonon spectrum in other classes of solid-state materials, such as thermoelectrics [25,26], hydrides [27], frustrated magnets [28], perovskites, and ceramic materials [29,30]. However, these pressure-induced changes on phonons and vibrations have never been directly measured in MNMs.

In this work, we focus on a prototypical air-stable Dy-based SMM: $[Dy(H_2O)_5(HMPA)_2]I_3 \cdot 2HMPA$ (HMPA = $[(CH_3)_2N]_3PO$). The system is characterized by a close-to-ideal pentagonal bipyramidal geometry, which promotes a strong axial CF and a sizable anisotropy barrier [31]. Being one of the few high-performance air-stable Ln-based SMMs, this system represents a good candidate for studying relaxation in applied hydrostatic pressure. The temperature-dependent relaxation dynamics of the system is interpreted within a DFT-based *cost-effective* theoretical framework [16]. This method, specifically developed for Ln-based SMMs, is able to give the physical insight inaccessible with the widely used phenomenological models, without being as demanding as fully *ab initio* calculations. Among the key ingredients of this method, there are CF Hamiltonian parameters and the phonon density of states (pDOS). The latter are efficiently calculated with periodic DFT starting from single-crystal x-ray diffraction data (see Table S1 in the Supplemental Material [32]), and validated through a demanding inelastic neutron scattering (INS) experiment on a molecular single crystal under applied hydrostatic pressure. Our theoretical approach accurately reproduces the measured temperature dependence on the relaxation rates of this SMM and the observed interplay between Raman and Orbach processes at ambient pressure, setting the starting point for the evaluation of the effects of pressure on the relaxation dynamics of the system. The significant reduction of the axial character of the calculated CF (see the Supplemental Material [32]) is responsible for both the promotion of the relaxation mechanisms involving the coupling with acoustic and low-energy optical phonons at intermediate temperatures, and for the enhancement of the QTM at low temperature (in accordance with Ref. [24]). We also find that low-lying phonon energies are considerably altered as a consequence of the applied pressure, and deviate from the canonical Debye picture for the pDOS. All these aspects result in a considerable predicted increase of the relaxation rate for the perturbed system.

II. RESULTS AND DISCUSSION

The mononuclear dysprosium-based SMM $[Dy(H_2O)_5(HMPA)_2]I_3 \cdot 2HMPA$ (**1**, with HMPA = hexamethylphosphoramide, $[(CH_3)_2N]_3PO$) was recently reported among the best performing air-stable SMMs [31]. The Dy^{III} ion is coordinated by five water ligands based on O51–O55, which form a close to ideal pentagonal bipyramidal coordination geometry (D_{5h}), capped above and below the plane by the oxygen atoms (O1 and O2) of the HMPA ligands, which promote a prominent axial CF (see Fig. 6(a) and Fig. S1 in the Supplemental Material [32]) [31]. When hydrostatic pressure is applied to the system, crystallographic investigations of the molecule with x-ray diffraction (see the Supplemental Material [32]) reveal a gradual deformation of the molecular structure. The overall pentagonal bipyramidal coordination polyhedron decreases slightly in volume from 19.32(17) Å^3 at ambient pressure to 18.7(3) Å^3 at 1.1 GPa [33]. Although the distance between Dy1 and O1 and O2 bonds does not appear to be sensitive to pressure in the range 0–1.1 GPa, the distances to the water ligands decrease slightly on average from 2.36 to 2.33 Å.

The most significant deformation is found for the axial O1–Dy1–O2 bond angle, which becomes markedly less linear, decreasing from 177.2(7)° to 171.0(9)° [see Fig. 6(b)]. The maximum deviation from the mean plane of the pentagonal moiety consisting of Dy1 and O51–O55 increases from 0.025(17) Å for O53 at ambient pressure to 0.15(2) Å for O52 at 1.1 GPa. Additionally, the bending in the O1–Dy1–O2 axis results in decreases in the angles made by O1 and O2 with equatorial pentagon from 89.7(5)° and 87.5(6)° at ambient pressure to 84.8(8)° and 86.2(8)° at 1.1 GPa. Finally, the angles subtended at Dy1 by pairs of water ligands do not deviate by more than 1.5° [34].

The general model Hamiltonian for SMMs like **1** can be written in the form

$$H = H_m + H_{\text{phonons}} + H_{\text{magnetoelastic}}. \quad (1)$$

The magnetic Hamiltonian $H_m = H_{\text{CF}} + H_{\text{Zeeman}}$ contains crystal field terms for the Dy^{3+} ion ($J = 15/2$) expressed in terms of Stevens operator equivalents $H_{\text{CF}} = \sum_{k,q} B_k^q O_k^q$ and a Zeeman contribution when an external field is applied $H_{\text{Zeeman}} = g_J \mu_B \boldsymbol{B} \cdot \boldsymbol{J}$. The CF parameters are calculated *ab initio* with the SINGLE_ANISO module of MOLCAS8.2 (see Tables S2–S4 in the Supplemental Material [32]) [35,36] and validated by comparing the magnetic susceptibility χ, measured as a function of temperature by dc magnetometry (see Fig. S2 in the Supplemental Material [32]), with the one calculated from the *ab initio* model Hamiltonian H_m. The eight Kramers doublets from the $^6H_{15/2}$ state span within an energy range of 614.1 cm^{-1} (76 meV) in ambient pressure, decreasing to a total span of 537.4 cm^{-1} (66.6 meV) at 1.1 GPa, with a consequent decrease of the gap between the $|\pm 15/2\rangle$ ground state and the first excited $|\pm 13/2\rangle$ from 293.8 cm^{-1} (36.4 meV) to 215.6 cm^{-1} (26.7 meV). Applied pressure indeed yields a reduction of the axial character of the CF, with a strong increase of the B_2^2 term, which becomes comparable with the B_2^0 one. We expect this to play a crucial role in QTM (see Sec. II D).

Additionally, Eq. (1) includes the H_{phonons} term for phonons, calculated with DFT (*vide infra*). The last term of the Hamiltonian, $H_{\text{magnetoelastic}} = \zeta_a H_{Jp}^{(a)} + \zeta_o H_{Jp}^{(o)}$, describes the magnetoelastic couplings of the spin degrees of freedom with acoustic ($H_{Jp}^{(a)}$) and optical ($H_{Jp}^{(o)}$) phonons, with $\zeta_{a,o}$ coupling coefficients.

A. Phonon-assisted relaxation mechanisms

The dependence on temperature of the relaxation dynamics of SMMs is governed by mechanisms involving the coupling of angular momentum with phonons and vibrations, where low-energy dispersive modes drive nonresonant Raman processes and optical ones trigger resonant Orbach relaxation. Indeed, in Ln-based SMMs with strong axial CF splittings, Orbach processes typically involve transitions between CF states separated by large energy gaps matching the frequencies of high-energy optical modes. In particular, it has been shown that the efficiency of Raman processes is crucial in determining the blocking temperature of Ln-based SMMs [5,16], making the pDOS an essential piece of information to capture their relaxation behavior. Both Raman and Orbach relaxation processes can be described within a cost-effective approach [16], combining *ab initio* calculations of the CF parameters and of the pDOS, with the fitting of only three microscopic parameters. This method allowed us to obtain a reliable model for the relaxation dynamics in SMMs in different temperature ranges, together with a well-defined hierarchy of the relaxation mechanisms [16]. In the intermediate temperature regime, the system dynamics is mainly restricted to the ground Kramers doublet of the $J = 15/2$ multiplet and excited CF states contribute to relaxation only via nonresonant Raman processes, driven by low-energy dispersive modes [37,38]. Thus, $H_{Jp}^{(a)}$ can be reasonably approximated by a "rotational Debye model" [39–42] and the relaxation rate becomes proportional to the integral

$$\int_0^\infty dE \frac{e^{E/k_BT}}{(e^{E/k_BT}-1)^2}\rho(E)\rho(E+\Delta)|M|^2, \tag{2}$$

where $\rho(E)$ is the pDOS and Δ is the Zeeman gap for the ground-state doublet. The term $|M|^2$ represents the matrix elements of the magnetoelastic couplings $H_{Jp}^{(a,o)}$. Although calculated over the whole phonon spectrum, Raman relaxation is driven mainly by low-energy dispersive modes, because of the T-dependent exponentials. In addition, the details on individual phonon modes are lost and, thus, phonon-induced Raman relaxation mainly depends on the low-energy profile of the pDOS only [5,39].

At higher temperatures, relaxation is driven by Orbach processes involving also excited doublets of the $J = 15/2$ multiplet, induced by optical phonon modes resonant with the CF gaps. Here, relaxation dynamics is described within a master equation approach where the rate matrix for the transition $t \to s$ is calculated as

$$W_{s\leftarrow t} = \frac{2\pi}{\hbar}\zeta^2\rho(\Delta E_{st})n(\Delta E_{st})|\langle s|V_1|t\rangle|^2. \tag{3}$$

The energy $\Delta E_{st} = E_s - E_t$ corresponds to the gap between two eigenstates $|s\rangle$ and $|t\rangle$ of the magnetic Hamiltonian H_m. The rate matrix depends linearly on the pDOS at the energy resonant with the CF gap $\rho(\Delta E_{st})$ and on the Bose-Einstein factor, written as $n(x) = (e^{x/k_BT} - 1)^{-1}$. The potential $V_1 = \sum_\Gamma \sum_{k,q} \eta_\Gamma^{k,q} O_k^q$ describes the modulation of the crystal field operators induced by the optical phonon modes Γ. Here, for simplicity, we assume a uniform coupling η independent of Γ, k, q. We have checked that a different choice (e.g., a random distribution of $\eta_\Gamma^{k,q}$) does not significantly alter our results. Indeed, Orbach relaxation is only influenced by the average value of the couplings η and by the phonon DOS at energies corresponding to CF gaps, allowing us to assume the same spin-phonon coupling for all the nondispersive modes.

In this work, the cost-effective approach is also employed to predict whether and how the pressure-induced modifications of the CF and vibrations impact spin relaxation.

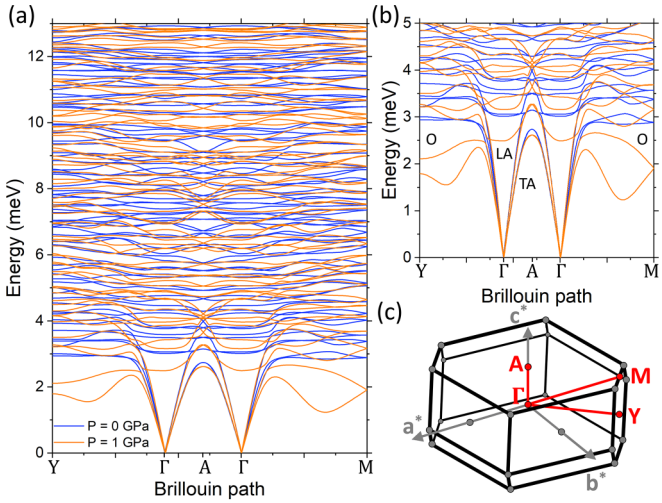

FIG. 1. (a) Periodic DFT calculation of the acoustic and optical phonon dispersion at ambient pressure (blue) and at 1 GPa (orange), over the path Y-Γ-A-Γ-M in the reciprocal space. (b) Close-up view of the lowest-lying phonon modes, highlighting pressure-induced changes in the low-energy region, where the transverse acoustical modes (TA) are bent toward lower energies and optical (O) and transverse and longitudinal acoustic modes (TA and LA, respectively) are significantly mixed by the anticrossings. (c) Reciprocal lattice cell with the symmetry points considered for the calculations in panel (a).

B. Investigation of low-energy phonon modes

As evidenced in Eqs. (2) and (3), it is essential to access information on the pDOS to evaluate the effect of the coupling with phonons on the magnetization relaxation dynamics. Phonon dispersions and pDOS of **1** at different applied pressures are thus calculated *ab initio* with periodic density functional theory (pDFT) (see Appendix A). The simulated phonon dispersions along the Y-Γ-A-Γ-M path in the reciprocal space [symmetry directions $(0k0)$, $(00l/2)$, and $(0kl/2)$, respectively, in conventional cell notation], are shown in Fig. 1 at ambient and applied $P = 1$ GPa hydrostatic pressure.

Phonon dispersions present the typical features of molecular crystals. Due to the presence of soft coordination bonds, these systems are characterized by the presence of dispersive optical modes at very low energy. These modes are indeed

strongly mixed with the acoustic ones due to the presence of several anticrossings and correspond to collective vibrations with little bond stretching. It has already been demonstrated that these dispersive low-energy modes are critically coupled to the spin [43,44] and play a pivotal role in the relaxation dynamics triggered by Raman mechanisms [16]. The effect of applied pressure to the phonon dispersion consists in a notable shift of the low-lying branches. The higher-energy longitudinal acoustic mode is slightly affected by pressure and only at the zone boundaries. Conversely, the energy of the two transverse acoustic modes is lowered, together with the lowest-lying optical modes (originally around 3 meV) down to 2 meV. These pressure-induced modifications of the spectrum also yield anticrossings between these modes at very low energies (at about 3 meV) and very close to the Γ point. The dispersion curves of these lowest-lying modes in applied pressure also show more accentuated bendings with respect to ambient pressure (see, for instance, those involving the higher-energy transverse acoustic mode and the lowest-lying optical mode along both Γ-Y and Γ-M directions highlighted in Fig. 1(b), indicating a stronger mixing induced by the anticrossings. By inspecting the optical modes at higher energies ($\geqslant$4 meV), the effect of pressure does not follow a specific trend, with an overall increase toward higher energies. The pressure-induced effects on the low-energy optical modes of **1** also affect the profile of the simulated pDOS shown in Fig. 2. The pDOS shows a general shift of the density of phonon modes toward higher energies in the range below 50 meV [see Fig. 2(a)], while the DOS profile at higher energies is mostly not affected by pressure. However, by inspecting the very low energy range, it is evident that when the external pressure is applied, the pDOS deviates from the canonical Debye-profile $\sim\omega^2$ toward a less steep trend [inset of Fig. 2(a)], convoluted with a complex structure due to the abundance of very low-energy-optical modes [see the high resolution Fig. 2(b)].

To validate the description of phonon and vibrations obtained with pDFT, we performed an INS experiment on **1**. Measurements were performed on both powders and single-crystal samples (all nondeuterated) on the thermal neutron spectrometer IN8 [45] at the Institute Laue-Langevin (ILL) (see Appendix B for more details, data available in Ref. [46]). The measurements on powder samples enabled the determination of the neutron-weighted phonon density of states (nw-pDOS) for **1** (see Appendix C). In Fig. 3, we compare the nw-pDOS measured at $T = 77$ K for two different $|\vec{Q}|$ values, with pDFT results obtained by calculating the atom-projected DOS and reconstructing the nw-pDOS within the one-phonon incoherent approximation (see Appendix C).

The good agreement between the calculated nw-pDOS and the INS data demonstrates the reliability of our *ab initio* approach for the pDFT. Indeed, calculations reproduce both the measured spectral features and the corresponding intensity in the whole explored energy regime [47].

To investigate the effect of pressure on phonons, we measure the energy dependence on the inelastic scattering function $S(\vec{Q}, E)$ of **1** at ambient and applied pressure ($P_0 =$ 0 GPa and $P_1 = 1$ GPa, respectively) with single-crystal measurements. A blank measurement of the sample environment is also performed and then subtracted from the data to extract the contribution of **1** to the scattering function (see

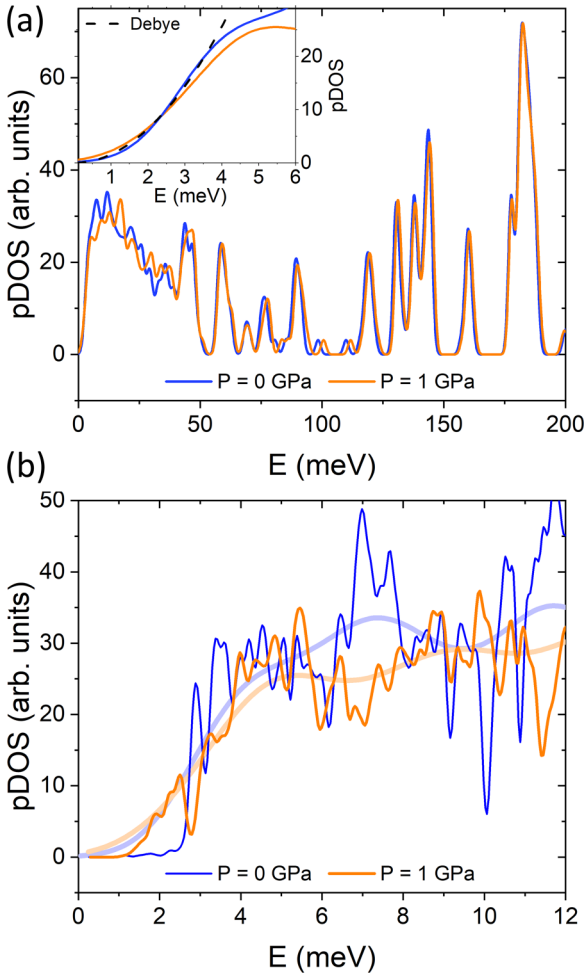

FIG. 2. (a) Periodic DFT calculations of the low-energy pDOS of **1** at ambient pressure (blue) and at 1 GPa (orange) with a fixed full width at half maximum (FWHM) of 1 meV. The effect of the applied pressure is particularly evident at low energy, where several features of the pDOS profile are shifted to higher energy. In inset, the observed deviation from the canonical quadratic Debye trend when the external pressure is applied. (b) A close up of the very-low-energy profile of the pDOS, calculated with higher resolution (FWHM of 0.08 meV), highlights instead the shift toward lower energies of the first optoacoustical modes with pressure, observed also in phonon dispersion.

Appendix B). The Γ-point energy scans were collected at a temperature of 77 K and are shown in Figs. 4(a) and 4(b). Data at ambient pressure show a sharp peak around 6.5 meV, which in applied pressure becomes less intense and broader. At $P_1 = 1$ GPa, the INS spectrum shows an overall spreading of the intensity with respect to ambient pressure, which might be due to pressure-induced broadening and inhomogeneous strain of the Hamiltonian parameters, with the exception of one defined feature emerging at about 18 meV.

INS experimental data [48] on single crystals of **1** are compared with the one-phonon coherent scattering function calculated starting from eigenvalues $\omega_s(\vec{q})$ and eigenvectors $\sigma_s(\vec{q})$ of the pDFT-calculated phonon modes (see Appendix A). From the comparison, it is evident that the calculations are consistent with INS data, in both ambient and

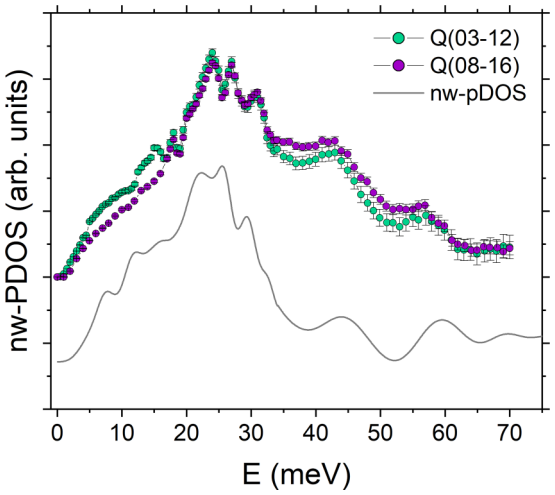

FIG. 3. Comparison between the nw-pDOS measured with INS (dots) at $\vec{Q}_1 = (0\ 3\text{–}12)$ and $\vec{Q}_2 = (0\ 8\text{–}16)$, expressed in terms of reciprocal lattice vector units ($|\vec{Q}| = 3.9$ and $5.6\,\text{Å}^{-1}$) and the one calculated with pDFT (gray line), convoluted with the experimental resolution of ∼1 meV in the range from 0 to 35 meV and ∼3 meV in the range from 35 to 70 meV.

applied pressure. It is worth noticing that a CF excitation from the ground state is also expected in both ambient and applied pressure cases, in the range between 25 and 35 meV, yielding an additional inelastic magnetic signal, superimposed to the one-phonon coherent scattering one. Despite the expected weakness of the magnetic signal with respect to the strong phonon one [49], calculations show that the phonon contribution in that energy range is not giving peaks and not expected to change with pressure. The fact that in the experimental spectrum, there seems to be instead a broad peak that changes with pressure close to the expected value for CF excitation (star symbols in Fig. 4) can be consistent with our proposition of its magnetic origin.

The substantial agreement between INS data and calculations confirms the reliability of our pDFT results on **1**.

C. Relaxation dynamics

The relaxation rate τ of sample **1** was investigated at ambient pressure by ac susceptibility measurements, in Ref. [31]. Two distinct relaxation regimes are clearly identified: At intermediate temperatures, the relaxation is dominated by nonresonant Raman processes, whereas at higher temperatures it is primarily governed by resonant Orbach processes. To simulate these experimental results, the phonon-induced relaxation rate was calculated using the theoretical framework described above. It is worth emphasizing that only three fitting parameters are considered: the coupling coefficients $\zeta_{a,o}$ with acoustic/optical modes and the upper energy limit for the rotational Debye description $\hbar\omega_D$. In molecular crystals, many low-energy optical modes maintain a significantly dispersive nature, and thus the upper energy limit $\hbar\omega_D$ can be reasonably used as a fitting parameter, in order to include all low-energy dispersive modes effectively contributing to Raman relaxation.

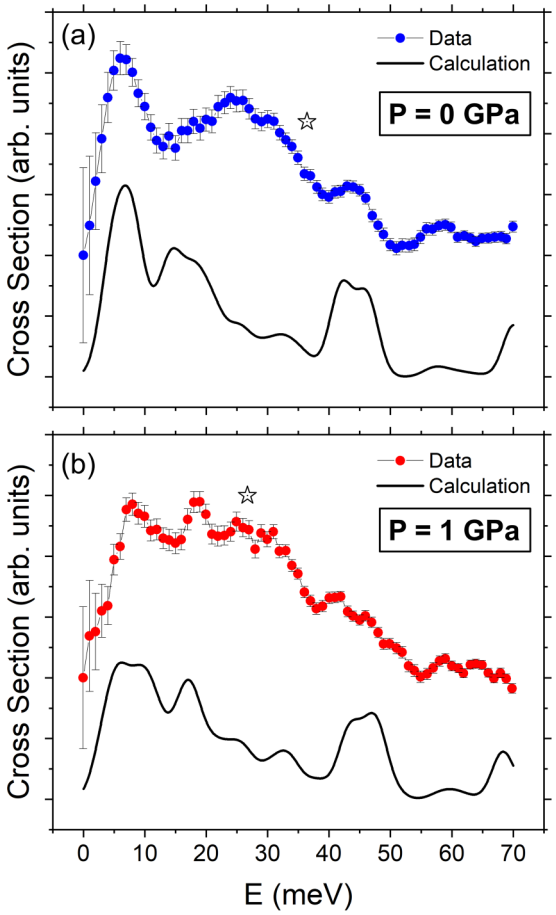

FIG. 4. Inelastic scattering function $S(\vec{Q}, E)$ measured at $\vec{Q}_1 = (0\ 3\text{–}12)$ for a fixed final wavevector $k_f = 4.11\,\text{Å}^{-1}$ and a resolution of ∼3 meV, in ambient [panel (a)] and applied hydrostatic pressure $P = 1$ GPa [panel (b)]. Blank measurements of the empty pressure cell have been subtracted from the data, to isolate the scattering contribution from the single crystal of **1**. Experimental data (dots) are compared with the coherent scattering function $S_{\text{coh}}(\vec{Q}, E)$ (black lines), calculated with the pDFT-calculated phonon frequencies $\omega_s(\vec{q})$ and polarization vectors $\sigma_s(\vec{q})$, and convoluted with the experimental resolution. A star dot indicates the range in which the first CF excitation is expected from CF calculations, in both pressure regimes.

The black line in Fig. 5 represents the combined contribution of both Raman and Orbach mechanisms to the relaxation rate at ambient pressure, calculated without assuming any phenomenological form. Our model is in excellent agreement with susceptibility data, assuming a Debye threshold energy of ≈4 meV. At intermediate temperatures (<25 K in Fig. 5), the results of the integral in Eq. (2) are compared with an effective power-law T dependence $\tau^{-1}_{\text{Raman}} = CT^n$ in a proper temperature range. This allows us to directly calculate the two parameters governing the relaxation rate in the Raman regime: the prefactor $C = 0.0015\ \text{K}^{-n}\,\text{s}^{-1}$ and an effective Raman exponent $n = 2.6$, mainly determined by the pDOS and the lowest CF energy gap. Furthermore, at higher temperature (above 25 K in Fig. 5), diagonalizing the rate matrix yields a single rate following an Arrhenius-like behavior $\tau^{-1}_{\text{Orbach}} = \tau_0^{-1} e^{-U_{\text{eff}}/T}$. Here, the model predicts an effective energy

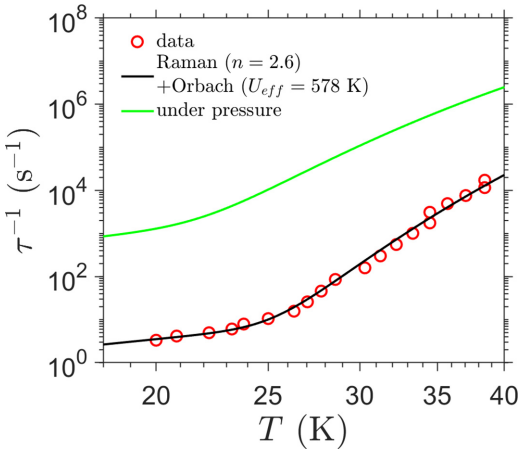

FIG. 5. Relaxation rate τ^{-1} of **1** measured from ac magnetometry (red dots) in ambient pressure conditions, as a function of temperature. Black line represents the simulated relaxation rate, comprising both Raman and Orbach contributions. Green line instead reveals the modeled increase of the relaxation rate τ^{-1} when the external pressure of 1 GPa is applied to the system.

barrier for multistep Orbach processes of $U_{\text{eff}} = 578$ K, which aligns well with previously reported values, determined by fitting ac-magnetometry data to an Arrhenius law [31].

The same method has been then used to predict the relaxation dynamics of **1** under an applied external pressure of 1 GPa (Fig. 5, green line). To account for the impact of pressure on all parameters used in the calculations, the magnetoelastic couplings were rescaled in accordance with the observed contraction of the crystal field spectrum, which shrank to approximately 87% of its original extension. The model reveals a large overall increase of the relaxation rate under pressure, with a less-steep Orbach regime that is activated at lower temperatures compared to the unperturbed case. The key parameters derived from the relaxation model include a strong increase of $C' = 0.29 \approx 190$ C, with practically unaffected Raman exponent, and a significant reduction of the energy barrier to $U_{\text{eff}} = 388$ K for the Orbach processes. These results are consistent with the observation outlined in Ref. [22] for an analogous Dy-based SMM.

D. Low-temperature quantum tunneling

For 4f-based SMMs, QTM under the barrier typically dominates over phonon-assisted mechanisms in prompting the relaxation dynamics in the low- temperature regime. Indeed, temperature-independent QTM is driven by fluctuations of local (internal+external) fields, which determine the onset of the resonant conditions between the two states of the ground doublet, $|\Uparrow\rangle$ and $|\Downarrow\rangle$. Once this resonance is met, tunneling occurs with a rate proportional to the square of the tunnel splitting. In Kramers systems such as Dy-based compounds, the latter is given by the off-diagonal element of the magnetic dipole J_α between $|\Uparrow\rangle$ and $|\Downarrow\rangle$ [50]. It is interesting to compare the values of $|\langle\Uparrow|J_\alpha|\Downarrow\rangle|$ obtained with the CF parameters computed *ab initio* at ambient pressure and at applied pressure of 1 GPa. Remarkably, we find that the application of the hydrostatic pressure enhances $|\langle\Uparrow|J_\alpha|\Downarrow\rangle|$ by a factor $\sim$24, consistent with the significantly accelerated tunneling dynamics observed in the hysteresis cycles (see Fig. 6), and with other examples in the literature [24]. This enhancement is attributable to the reduction of the axial character of the CF, witnessed by the increased B_2^2 term. The latter gains several orders of magnitude when the pressure is applied, becoming

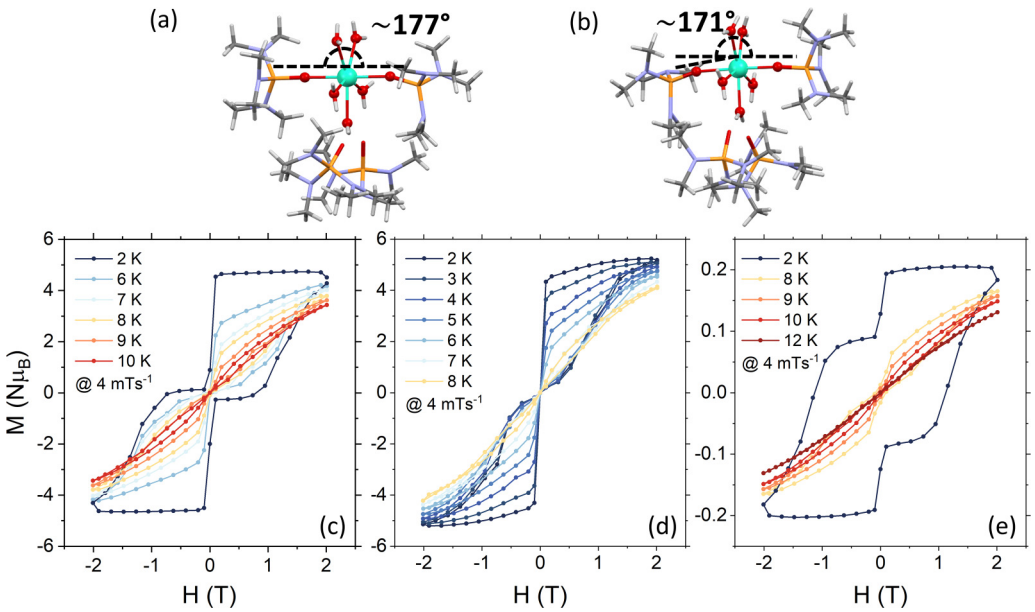

FIG. 6. (a) Molecular structure of $[Dy(H_2O)_5(HMPA)_2]I_3 \cdot 2$ HMPA at ambient pressure. (b) Molecular structure variation, induced by an applied pressure of 1.1 GPa, showing the reduced axial angle from 177° (at ambient pressure) to 171°. (c), (d) Field-dependent dc magnetization measurements $M(H)$ for two different applied hydrostatic pressures [ambient pressure panel (c), 1.1 GPa panel (d)] of a powder sample of **1**. (e) Field-dependent dc magnetization measurements M(H) for diluted sample of **1** in its Y-diamagnetic analog under ambient pressure. Panels (c) and (e) are reproduced from Ref. [31] with permission from the Royal Society of Chemistry.

comparable in magnitude to the axial term B_2^0, previously dominant in ambient pressure (see Table S1 in the Supplemental Material [32]).

Field-dependent dc magnetization measurements at low temperatures were performed on powder samples of **1** and of its 5% Dy-doped Yttrium analog (**1′**), with an average sweep rate of ∼4 mT s^{-1}. Magnetic hysteresis is observable up to $T = 9$ K for **1** and $T = 10$ K for **1′**, at ambient pressure. When a hydrostatic pressure of 1.1 GPa is applied, the nondiluted sample shows no open hysteresis even at 2 K. Moreover, at ambient pressure, **1** shows butterfly-shaped hysteresis loops down to 2 K, suggesting the occurrence at near-zero applied field of fast QTM processes, not completely suppressed by the axial symmetry of the complex [Fig. 6(d)]. The effects of QTM are indeed less pronounced in the low-temperature hysteresis cycles of **1′** [Fig. 6(c)], confirming the role played by internal dipolar fields in inducing tunnel splittings.

When a hydrostatic pressure is applied to the system, x-ray diffraction evidences a gradual deformation of the ligand's axial angle, with a consequent loss of axiality. This pressure-induced deviation from perfect axial symmetry introduces transverse CF terms, which, combined with presence of small transverse magnetic fields and hyperfine coupling with nonzero nuclear spins breaking the Kramers degeneracy [5], open tunneling pathways between the two orientations of the ground doublet, thus enabling QTM even at zero external magnetic field. Consequently, the field-dependent magnetization curves change significantly under applied pressure, exhibiting a more pronounced QTM step near zero field than that observed in Fig. 6(c) at the same temperature in ambient pressure. Thus, at 1.1 GPa, the tunneling dynamics become more effective in promoting relaxation even at zero external magnetic field, restoring a butterfly-shaped hysteresis loop down to very low temperatures ($T = 2$ K) [see Fig. 6(d)]. These magnetometry results in applied pressure are in line with the matrix element for the QTM channels calculated above. Indeed, the loss of axiality evidenced by x-ray diffraction and in *ab initio* CF parameters is expected to enhance the tunneling dynamics.

III. CONCLUSION

To improve the relaxation performance of molecular nanomagnets, it is essential to comprehend the interplay of various mechanisms that govern their relaxation dynamics. Valuable insights can be obtained by comparing the performances of different compounds, whose differences could, however, prevent a complete disentanglement of the role played by various ingredients. The investigation of MNMs under modified environmental conditions, such as applied external pressure, represents an alternative route to gain the same insight. Indeed, pressure alters both the phonon spectrum and CF of the molecule, with the advantage of preserving the main characteristics of the molecular structure.

For the mononuclear Dy-based SMM (**1**) studied in this work, we predict that the application of an external pressure should lead to a much faster relaxation of the magnetization. The effects of pressure on the CF and on the phonon spectrum of the molecule have been experimentally assessed in this work. On one hand, x-ray diffraction and magnetometry measurements allowed us to estimate the loss of axiality of the CF due to pressure, leading to an enhancement of the QTM as evidenced, for instance, in hysteresis cycles. On the other hand, INS experiments provided us, for the first time, a picture of phonons under pressure, with the lowest-energy modes being the most affected.

With the support of our theoretical approach, we have also predicted that the modifications induced on the CF axiality provide the most significant contribution to the overall acceleration of the relaxation dynamics, dominating over the effects due to changes in the phonon spectrum. Indeed, not only does the loss of CF axiality due to pressure foster QTM, but it also makes phonon-induced processes faster, with significant changes in the magnetoelastic matrix elements, leading to an increase in the Raman prefactor $C' = 0.29 \approx 190\,\mathrm{C}$. Moreover, the variation of the crystal field yields a decrease in the Orbach U_{eff} from 589 to 388 K. The results obtained in this work demonstrate that the combination of different experimental techniques, such as magnetometry and INS, allows for the disentanglement of the role played by CF axiality and phonons in MNMs relaxation dynamics and QTM. Applied pressure represents an additional tool to influence their interplay, highlighting the effects of one ingredient (CF axiality, in this case) over the other. These results, therefore, pave the way for a systematic approach to compare the performances of different SMMs with different molecular structures and therefore to improve the design of future systems.

ACKNOWLEDGMENTS

This work received financial support from the European Union-NextGenerationEU, PNRR MUR Project No. PE0000023-NQSTI, from the European Union's Horizon 2020 program under Grant Agreement No. 862893 (FET-OPEN project FATMOLS), from the Novo Nordisk foundation under Grant No. NNF21OC0070832 in the call "Exploratory Interdisciplinary Synergy Programme 2021" and from the UK Engineering and Physical Sciences Research Council, under Grant No. EP/N01331X/1, and the University of Glasgow and from SERB/ANRF India (CRG/2022/001697). We acknowledge the Institute Laue-Langevin, instrument IN8, for the INS measurements (proposal 89842) the STFC (Science & Technology Facilities Council) Scientific computing Department's SCARF High Performance Computing cluster and the CINECA Supercomputing Centre (CINECA ISCRA initiative) for the high-performance computing resources and support and Diamond Light Source for time on Beamline I19 under Proposal MT16139-3 and Dr. Mark Warren for his assistance during the experiment.

DATA AVAILABILITY

The data that support the findings of this article are openly available [51].

APPENDIX A: PERIODIC DFT CALCULATIONS

pDFT calculations were performed using the QuantumESPRESSO package [52–54], which uses a plane wave basis set

and pseudopotentials. The energy cutoff for the wavefunctions was set to 1225 eV, while the reciprocal space integration was performed with a $2 \times 2 \times 1$ Monkhost-Pack [55] grid when considering the primitive unit cell. The optimized norm-conserving vanderbilt pseudopotentials (ONCV) [56] were used for all elements, and the exchange and correlation contribution was described with the Perdew, Burke, and Ernzerhof (PBE) functional [57] and the nonlocal vdW-DF functional in order to include van der Waals (vdw) interactions [58–62]. All atomic positions were optimized until atomic forces were smaller than 2.57×10^{-4} eV Å^{-1} and total energy differences among optimization steps were smaller than 2 meV, while the experimental lattice parameters were kept fixed during the relaxation. Phonon frequencies were obtained with the Phonopy package [63]. In this case, a $2 \times 2 \times 1$ supercell is used to collect the interatomic force constants by performing 0.011 Å position displacements. The reciprocal space is sampled using only the Γ point in this latter case. The starting crystallographic cell has been adapted to each pressure condition and verified by comparison with x-ray diffraction data under the same conditions (see the Supplemental Material [32]).

APPENDIX B: INELASTIC NEUTRON SCATTERING EXPERIMENT

The inelastic neutron scattering experiment was performed at ILL on the thermal neutron triple-axis spectrometer IN8 [45]. This high incident flux spectrometer is optimized for the characterization of lattice vibrations and magnetic excitations in the range from 0 to ∼100 meV, for sample of small volume and weak signals. We exploited a Si (111) monochromator, in combination with a PG (002) analyser with a fixed final wavevector of $k_f = 2.66$ Å^{-1}, featuring a nominal resolution of ∼1 meV for the energy range from 0 to 35 meV and a pyrolytic graphite monochromator PG (002), in combination with a PG (002) analyser with a fixed final wavevector of $k'_f = 4.11$ Å^{-1}, featuring high flux and a nominal resolution of ∼3 meV for the higher energies. Higher-order contaminations in the monochromatic beams 111 were practically entirely removed with an oriented pyrolytic graphite filter. A powder sample of **1** was prepared in a thin aluminum cylinder, screwed on the cryostat probe to set the measuring temperature at 77 K. The pDOS has been measured for two different scattering vectors $|\vec{Q}|$. When measuring INS spectra from a powder sample, information about the orientation of the scattering vector relative to the crystal structure is lost due to the averaging over all the orientations. In this case, the relevant quantity is the incoherent scattering function $S_{\text{incoh}}(\vec{Q}, \omega)$, which is proportional to the Fourier transform of the self-correlation function $\propto \sum_i \langle e^{-i\vec{Q}\cdot\vec{R}_i(0)}\, e^{i\vec{Q}\cdot\vec{R}_i(t)}\rangle$, describing the motion of the same atom i at different times t [64–66]. This self-scattering term is the one that contributes to the incoherent part of the scattering cross section.

By averaging over the distribution of orientation, the dependence of the scattering intensity on the wavevectors $\vec{Q}$ and polarization states s is lost and thus, the scattering function $S_{\text{incoh}}(\vec{Q}, E)$ (B1) only depends on the number of phonon modes ($3N$ in total) satisfying $\delta(\omega \pm \omega_s(\vec{q}))$ (with ω_s frequency of the normal modes of a quantum harmonic oscillator) and can be described in the so-called incoherent approximation, where it results directly proportional to the neutron weighted phonon density of states $\rho_{nw}(\omega)$ (*vide infra*) [64–66]:

$$S_{\text{incoh}}(Q, \omega) \propto e^{-2W(Q)} \frac{Q^2}{\omega} \rho_{nw}(\omega)[(n_s(\vec{q}) + 1)]. \tag{B1}$$

Here, working in neutron energy loss configuration, the Bose-Einstein occupancy factor $[(n_j(\vec{q}) + 1) + n_j(\vec{q})]$ is reduced to $[(n_j(\vec{q}) + 1)]$. Additionally, $e^{-2W(\vec{Q})}$ is the term accounting for the Debye-Waller effect. It is worth noting that Dy and ^{1}H are the only nuclei in the system with significant incoherent cross sections [64]. Consequently, these elements dominate the powder experimental spectrum, with ^{1}H in particular playing the major role due to its abundance in the molecule and its exceptionally large incoherent scattering cross section.

IN8 can also be equipped with a high-pressure Paris-Edinburgh cell [67] that can emulate the pressure applied for the magnetometry experiments in Sec. II D (0 and 1.1 GPa). Due to the chemical incompatibility of the single crystal of **1** with the liquid vectors commonly used to apply hydrostatic pressure, we devised an alternative approach employing lead filings as a vector to distribute uniformly the external pressure. The crystal was placed inside a CuBe gasket of the Paris-Edinburgh cell, the empty spaces have been closed with the lead filings and then pressed to a gapless pocket. The Paris-Edinburgh cell was then inserted into a He cryostat. Due to the large mass of the cell, cooling was accelerated by introducing liquid nitrogen into the cryostat's calorimeter to bring the system efficiently down to 77 K. Since lower temperatures were not required for our study, we maintained the system at this temperature to avoid unnecessary downtime. The energy scans on single crystals were collected by exploiting the PG (002) monochromator and the PG (002) analyser with fixed $k_f = 4.1$ Å^{-1} configuration (∼3 meV resolution), to maximize the neutron flux in the energy range 0–70 meV.

When the INS experiment is performed on oriented single crystals, the phase relationships between scattering from different atoms i and i' at different times t are preserved. As a result, the scattering cross section is dominated by the coherent scattering function $S_{\text{coh}}(\vec{Q}, \omega)$, which is proportional to the Fourier transform of the correlation function $\sum_{i,i'} \langle e^{-i\vec{Q}\cdot\vec{R}_i(0)}\, e^{i\vec{Q}\cdot\vec{R}_{i'}(t)}\rangle$. In this case, the dependence of the scattering intensity on both the wavevector $\vec{Q}$ and the polarization states s is preserved, and the spectral features observed at specific reciprocal-space vectors $\vec{Q}$ directly reflect collective excitations, such as phonons, and their dispersion relations [64–66]. Again, due to its much greater abundance, comparable coherent scattering cross section and lighter mass [which appears in the denominator of Eq. (C2)], the contribution of ^{1}H will also dominate the coherent scattering cross section.

APPENDIX C: DATA ANALYSIS AND SIMULATIONS

Neutron scattering data were treated in order to extract the experimental nw-pDOS and the inelastic cross section, to be compared directly with calculations obtained from p-DFT. The nw-pDOS, after normalization for the monitor counts, has been extracted directly from the definition (B1) of the

one-phonon incoherent scattering function $S_{\text{incoh}}(\vec{Q}, E)$, as

$$\rho_{nw}(\omega) \propto \frac{\omega S_{\text{incoh}}(\vec{Q}, E)}{Q^2 e^{-2W(\vec{Q})}(n_s(\vec{q}) + 1)}. \tag{C1}$$

The nw-pDOS $\rho_{nw}(\omega) = \sum_d \frac{\sigma_s(d)}{2M_d}\rho_d(\omega)$ depends on the partial density of states $\rho_d(\omega)$ weighted by the scattering cross section σ_s and mass M_d of each element d in the compound. To reproduce the measured INS data, we performed pDFT simulations to calculate the partial DOS $\rho_d(\omega)$ for each element and reconstruct the nw-pDOS.

Instead, simulations of the Γ-point one-phonon coherent scattering function (for the neutron energy-loss configuration) [64–66]

$$S_{coh}(\vec{Q}, \omega) \propto \left(\frac{1}{2m_n}\right) \sum_{\vec{\tau}} e^{-2W(\vec{Q})} \sum_{s\vec{q}} \frac{|\vec{Q} \cdot \vec{\sigma}_s(\vec{q})|^2}{\omega_s(\vec{q})} \times [(n_s(\vec{q}) + 1)\delta(\omega - \omega_s(\vec{q}))\delta(\vec{Q} - (\vec{\tau} + \vec{q}))] \tag{C2}$$

were performed by exploiting phonon energies $\omega_s(\vec{q})$ and normal modes polarization vectors $\vec{\sigma}_s(\vec{q})$ calculated with pDFT both in ambient and applied pressure. The obtained cross section was then convoluted with a reasonable Gaussian resolution function with FWHM ∼ 4 meV. This line width allows us to compare our calculations with the experimental data across the whole energy range explored, considering an additional broadening attributed to the complex sample environment. In order to extract the inelastic coherent scattering function from the sample $S_M^{j,j'}(\vec{Q}, E)$ of Eq. (C2) from single-crystal neutron data $S_{\text{exp}}^{j,j'}(\vec{Q}, E)$, which also include contributions from the gasket and the pressure cell, we subtracted a blank measurement obtained from the sample environment without the sample ($S_{\text{blank}}^{j,j'}(\vec{Q}, E)$). In addition, to correct for the different neutron absorbance (different lead filling mass), an appropriate weight η_{blank} that takes into account the self-shielding of the sample and the different mass of the lead was multiplied to the blank before the subtraction. An additional small Lorentzian quasielastic contribution $\mathcal{L}_{q-e}$ was also subtracted to the experimental cross section.

$$S_M^{j,j'}(\vec{Q}, E) \approx S_{\text{exp}}^{j,j'}(\vec{Q}, E) - \left[\eta_{\text{blank}}\left(S_{\text{blank}}^{j,j'}(\vec{Q}, E)\right) + \mathcal{L}_{q-e}\right]. \tag{C3}$$

[1] R. Sessoli, D. Gatteschi, A. Caneschi, and M. A. Novak, Magnetic bistability in a metal-ion cluster, Nature (London) **365**, 141 (1993).

[2] A. Chiesa, T. Guidi, S. Carretta, S. Ansbro, G. A. Timco, I. Vitorica-Yrezabal, E. Garlatti, G. Amoretti, R. E. P. Winpenny, and P. Santini, Magnetic exchange interactions in the molecular nanomagnet Mn_{12}, Phys. Rev. Lett. **119**, 217202 (2017).

[3] C. A. P. Goodwin, F. Ortu, D. Reta, N. F. Chilton, and D. P. Mills, Molecular magnetic hysteresis at 60 Kelvin in dysprosocenium, Nature (London) **548**, 439 (2017).

[4] F.-S. Guo, B. M. Day, Y.-C. Chen, M.-L. Tong, A. Mansikkamäki, and R. A. Layfield, Magnetic hysteresis up to 80 kelvin in a dysprosium metallocene single-molecule magnet, Science **362**, 1400 (2018).

[5] A. Chiesa, F. Cugini, R. Hussain, E. Macaluso, G. Allodi, E. Garlatti, M. Giansiracusa, C. A. P. Goodwin, F. Ortu, D. Reta, J. M. Skelton, T. Guidi, P. Santini, M. Solzi, R. De Renzi, D. P. Mills, N. F. Chilton, and S. Carretta, Understanding magnetic relaxation in single-ion magnets with high blocking temperature, Phys. Rev. B **101**, 174402 (2020).

[6] A. H. Vincent, Y. L. Whyatt, N. F. Chilton, and J. R. Long, Strong axiality in a dysprosium (III) bis(borolide) complex leads to magnetic blocking at 65 k, J. Am. Chem. Soc. **145**, 1572 (2023).

[7] C. A. Gould, K. R. McClain, D. Reta, J. G. C. Kragskow, D. A. Marchiori, E. Lachman, E.-S. Choi, J. G. Analytis, R. D. Britt, N. F. Chilton, B. G. Harvey, and J. R. Long, Ultrahard magnetism from mixed-valence dilanthanide complexes with metal-metal bonding, Science **375**, 198 (2022).

[8] D. Gatteschi, R. Sessoli, and J. Villain, *Molecular Nanomagnets* (Oxford University Press, Oxford, UK, 2006).

[9] N. F. Chilton, Molecular magnetism, Annu. Rev. Mater. Res. **52**, 79 (2022).

[10] A. Chiesa, P. Santini, E. Garlatti, F. Luis, and S. Carretta, Molecular nanomagnets: A viable path toward quantum information processing? Rep. Prog. Phys. **87**, 034501 (2024).

[11] A. Gaita-Ariño, F. Luis, S. Hill, and E. Coronado, Molecular spins for quantum computation, Nat. Chem. **11**, 301 (2019).

[12] E. Moreno-Pineda, C. Godfrin, F. Balestro, W. Wernsdorfer, and M. Ruben, Molecular spin qudits for quantum algorithms, Chem. Soc. Rev. **47**, 501 (2018).

[13] M. N. Leuenberger and D. Loss, Quantum computing in molecular magnets, Nature (London) **410**, 789 (2001).

[14] S. Carretta, D. Zueco, A. Chiesa, A. Gómez-León, and F. Luis, A perspective on scaling up quantum computation with molecular spins, Appl. Phys. Lett. **118**, 240501 (2021).

[15] S. Chicco, G. Allodi, A. Chiesa, E. Garlatti, C. D. Buch, P. Santini, R. De Renzi, S. Piligkos, and S. Carretta, Proof-of-concept quantum simulator based on molecular spin qudits, J. Am. Chem. Soc. **146**, 1053 (2024).

[16] E. Garlatti, A. Chiesa, P. Bonfà, E. Macaluso, I. J. Onuorah, V. S. Parmar, Y.-S. Ding, Y.-Z. Zheng, M. J. Giansiracusa, D. Reta, E. Pavarini, T. Guidi, D. P. Mills, N. F. Chilton, R. E. P. Winpenny, P. Santini, and S. Carretta, A cost-effective semi-*ab initio* approach to model relaxation in rare-earth single-molecule magnets, J. Phys. Chem. Lett. **12**, 8826 (2021).

[17] D. Reta, J. G. C. Kragskow, and N. F. Chilton, *Ab initio* prediction of high-temperature magnetic relaxation rates in single-molecule magnets, J. Am. Chem. Soc. **143**, 5943 (2021).

[18] M. Briganti, F. Santanni, L. Tesi, F. Totti, R. Sessoli, and A. Lunghi, A complete *ab initio* view of Orbach and Raman spin–lattice relaxation in a dysprosium coordination compound, J. Am. Chem. Soc. **143**, 13633 (2021).

[19] A. Lunghi, Toward exact predictions of spin-phonon relaxation times: An *ab initio* implementation of open quantum systems theory, Sci. Adv. **8**, eabn7880 (2022).

[20] Y.-S. Ding, K.-X. Yu, D. Reta, F. Ortu, R. E. P. Winpenny, Y.-Z. Zheng, and N. F. Chilton, Field- and temperature-dependent quantum tunnelling of the magnetisation in a large barrier single-molecule magnet, Nat. Commun. **9**, 3134 (2018).

[21] S. Chicco, E. Garlatti, F. Cugini, R. E. Rheam, J. R. Travis, A. M. Hess, M. Zeller, M. Solzi, S. Carretta, and C. M. Zaleski, Slow relaxation of the magnetization in dysprosium–aluminum metallacrowns, ACS Omega **10**, 56096 (2025).

[22] V. S. Parmar, A. M. Thiel, R. Nabi, G. K. Gransbury, M. S. Norre, P. Evans, S. C. Corner, J. M. Skelton, N. F. Chilton, D. P. Mills, and J. Overgaard, Influence of pressure on a dysprosocenium single-molecule magnet, Chem. Commun. **59**, 2656 (2023).

[23] A. Sieber, R. Bircher, O. Waldmann, G. Carver, G. Chaboussant, H. Mutka, and H.-U. Güdel, Effect of pressure on the magnetic anisotropy in the single-molecule magnet Mn12-acetate: An inelastic neutron scattering study, Angew. Chem. Int. Ed. **44**, 4239 (2005).

[24] M. S. Norre, C. Gao, S. Dey, S. K. Gupta, A. Borah, R. Murugavel, G. Rajaraman, and J. Overgaard, High-pressure crystallographic and magnetic studies of pseudo-D_{5h} symmetric Dy(III) and Ho(III) single-molecule magnets, Inorg. Chem. **59**, 717 (2020).

[25] R. Cheng, X. Shen, S. Klotz, Z. Zeng, Z. Li, A. Ivanov, Y. Xiao, L.-D. Zhao, F. Weber, and Y. Chen, Lattice dynamics and thermal transport of PbTe under high pressure, Phys. Rev. B **108**, 104306 (2023).

[26] K. Yuan, Z. Sun, X. Zhang, and D. Tang, Tailoring phononic, electronic, and thermoelectric properties of orthorhombic GeS through hydrostatic pressure, Sci. Rep. **9**, 9490 (2019).

[27] V. E. Antonov, V. K. Fedotov, A. S. Ivanov, A. I. Kolesnikov, M. A. Kuzovnikov, M. Tkacz, and V. A. Yartys, Lattice dynamics of high-pressure hydrides studied by inelastic neutron scattering, J. Alloys Compd. **905**, 164208 (2022).

[28] K. V. Lawler, D. Smith, S. R. Evans, A. M. dos Santos, J. J. Molaison, J.-W. G. Bos, H. Mutka, P. F. Henry, D. N. Argyriou, A. Salamat, and S. A. J. Kimber, Decoupling lattice and magnetic instabilities in frustrated $CuMnO_2$, Inorg. Chem. **60**, 6004 (2021).

[29] C. Wang, Y. Liu, S. F. Liu, B. Li, and Y. Chen, Giant phonon tuning effect via pressure-manipulated polar rotation in perovskite $MAPbI_3$, J. Phys. Chem. Lett. **9**, 3029 (2018).

[30] R. Mittal, S. L. Chaplot, H. Schober, and T. A. Mary, Origin of negative thermal expansion in cubic ZrW_2O_8 revealed by high pressure inelastic neutron scattering, Phys. Rev. Lett. **86**, 4692 (2001).

[31] A. B. Canaj, M. K. Singh, C. Wilson, G. Rajaraman, and M. Murrie, Chemical and in silico tuning of the magnetization reversal barrier in pentagonal bipyramidal Dy(III) single-ion magnets, Chem. Commun. **54**, 8273 (2018).

[32] See Supplemental Material at http://link.aps.org/supplemental/10.1103/y7kz-8f3s for single crystal x-ray diffraction data, crystallographic structure, dc magnetometry data fitted with the cf spin Hamiltonian, and details on the calculated crystal field parameters, which includes Refs. [68–70].

[33] R. Angel, M. M., L. Baratelli, C. Schweinle, T. Balic-Žunic, J. Gonzalez-Platas, and M. Alvaro, Uncertainties of recalculated bond lengths, angles and polyhedral volumes as implemented in the crystal palace program for parametric crystal structure analysis, Acta Cryst. A **81**, 202 (2025).

[34] A. L. Spek, Single-crystal structure validation with the program PLATON, J. Appl. Cryst. **36**, 7 (2003).

[35] F. Aquilante, J. Autschbach, R. K. Carlson, L. F. Chibotaru, M. G. Delcey, L. D. Vico, I. F. Galván, N. Ferré, L. M. Frutos, and L. Gagliardi, Molcas 8: New capabilities for multiconfigurational quantum chemical calculations across the periodic table, J. Comput. Chem. **37**, 506 (2016).

[36] L. F. Chibotaru and L. Ungur, *Ab initio* calculation of anisotropic magnetic properties of complexes. I. Unique definition of pseudospin Hamiltonians and their derivation, J. Chem. Phys. **137**, 064112 (2012).

[37] K. N. Shrivastava, Theory of spin–lattice relaxation, Phys. Status Solidi B **117**, 437 (1983).

[38] A. Singh and K. N. Shrivastava, Optical-acoustic two-phonon relaxation in spin systems, Phys. Status Solidi B **95**, 273 (1979).

[39] L. T. A. Ho and L. F. Chibotaru, Spin-lattice relaxation of magnetic centers in molecular crystals at low temperature, Phys. Rev. B **97**, 024427 (2018).

[40] M. N. Leuenberger and D. Loss, Spin tunneling and phonon-assisted relaxation in Mn_{12}-acetate, Phys. Rev. B **61**, 1286 (2000).

[41] C. Calero, E. M. Chudnovsky, and D. A. Garanin, Two-phonon spin-lattice relaxation of rigid atomic clusters, Phys. Rev. B **74**, 094428 (2006).

[42] P. Thalmeier and B. Lüthi, *The Electron-Phonon Interaction in Intermetallic Compounds* (Elsevier, North Holland, Amsterdam, 1991), Chap. 96, pp. 225–341.

[43] E. Garlatti, L. Tesi, A. Lunghi, M. Atzori, D. J. Voneshen, P. Santini, S. Sanvito, T. Guidi, R. Sessoli, and S. Carretta, Unveiling phonons in a molecular qubit with four-dimensional inelastic neutron scattering and density functional theory, Nat. Commun. **11**, 1751 (2022).

[44] E. Garlatti, A. Albino, S. Chicco, V. H. A. Nguyen, F. Santanni, L. Paolasini, C. Mazzoli, R. Caciuffo, F. Totti, P. Santini, R. Sessoli, A. Lunghi, and S. Carretta, The critical role of ultra-low-energy vibrations in the relaxation dynamics of molecular qubits, Nat. Commun. **14**, 1653 (2023).

[45] A. Piovano and A. Ivanov, The TAS-IN8 upgrade: Towards the limit of a three-axis spectrometer performance, EPJ Web Conf. **286**, 03011 (2023).

[46] INS data measured on IN8 beamline, Available at: 10.5291/ill-data.7-01-566 (2021).

[47] At energies above 30 meV, we observe a more pronounced background in the experimental data with respect to calculations. Due to its broad nature, the observed signal can be attributed to a nonnegligible coherent contribution to the scattered intensity (not included in the incoherent approximation), or/and to multiphonon contributions at high energy, which are excluded in the one-phonon expansion of the neutron cross section.

[48] Experimental data are rebinned by a three-point moving average method.

[49] The comparison is expected to be less reliable in the region between 20 and 35 meV, where the pressure cell scattering cross section is steeper and the blank subtraction less effective.

[50] Due to the not fully axial CF in the present system, the magnetic dipole is purely off-diagonal for a direction intermediate between x and y axes.

[51] S. Chicco, E. Garlatti, A. Mavromagoulos, A. B. Canaj, P. Bonfà, A. Piovano, S. Dey, H. Little, A. Chiesa, A. S.

Ivanov, I. J. Onuorah, S. Parsons, G. Rajaraman, T. Guidi, M. Murrie, and S. Carretta, Dy-based single-molecule magnet as a case study for magnetization relaxation under applied pressure - open dataset [Data set], Zenodo (2025), doi:10.5281/zenodo.15310931.

[52] P. Giannozzi, O. Baseggio, P. Bonfà, D. Brunato, R. Car, I. Carnimeo, C. Cavazzoni, S. de Gironcoli, P. Delugas, F. Ferrari Ruffino, A. Ferretti, N. Marzari, I. Timrov, A. Urru, and S. Baroni, Quantum ESPRESSO toward the exascale, J. Chem. Phys **152**, 154105 (2020).

[53] P. Giannozzi, *et al.*, Advanced capabilities for materials modelling with quantum ESPRESSO, J. Phys.: Condens. Matter **29**, 465901 (2017).

[54] P. Giannozzi, *et al.*, Quantum ESPRESSO: A modular and open-source software project for quantum simulations of materials, J. Phys.: Condens. Matter **21**, 395502 (2009).

[55] H. J. Monkhorst and J. D. Pack, Special points for Brillouin-zone integrations, Phys. Rev. B **13**, 5188 (1976).

[56] D. R. Hamann, Optimized norm-conserving Vanderbilt pseudopotentials, Phys. Rev. B **88**, 085117 (2013).

[57] J. P. Perdew, K. Burke, and M. Ernzerhof, Generalized gradient approximation made simple, Phys. Rev. Lett. **77**, 3865 (1996).

[58] R. Sabatini, E. Küçükbenli, B. Kolb, T. Thonhauser, and S. de Gironcoli, Structural evolution of amino acid crystals under stress from a non-empirical density functional, J. Phys.: Condens. Matter **24**, 424209 (2012).

[59] D. C. Langreth, B. I. Lundqvist, S. D. Chakarova-Käck, V. R. Cooper, M. Dion, P. Hyldgaard, A. Kelkkanen, J. Kleis, L. Kong, S. Li, P. G. Moses, E. Murray, A. Puzder, H. Rydberg, E. Schröder, and T. Thonhauser, A density functional for sparse matter, J. Phys.: Condens. Matter **21**, 084203 (2009).

[60] K. Berland, V. R. Cooper, K. Lee, E. Schröder, T. Thonhauser, P. Hyldgaard, and B. I. Lundqvist, Van der Waals forces in density functional theory: A review of the vdW-DF method, Rep. Prog. Phys. **78**, 066501 (2015).

[61] T. Thonhauser, V. R. Cooper, S. Li, A. Puzder, P. Hyldgaard, and D. C. Langreth, Van der Waals density functional: Self-consistent potential and the nature of the van der Waals bond, Phys. Rev. B **76**, 125112 (2007).

[62] T. Thonhauser, S. Zuluaga, C. A. Arter, K. Berland, E. Schröder, and P. Hyldgaard, Spin signature of nonlocal correlation binding in metal-organic frameworks, Phys. Rev. Lett. **115**, 136402 (2015).

[63] A. Togo, F. Oba, and I. Tanaka, First-principles calculations of the ferroelastic transition between rutile-type and $CaCl_2$-type SiO_2 at high pressures, Phys. Rev. B **78**, 134106 (2008).

[64] G. L. Squires, *Introduction to the Theory of Thermal Neutron Scattering* (Cambridge University Press, Cambridge, UK, 2012), 3rd ed.

[65] A. T. Boothroyd, *Principles of Neutron Scattering from Condensed Matter* (Oxford University Press, Oxford, UK, 2020).

[66] W. Marshall and S. W. Lovesey, *Theory of Thermal Neutron scattering: The Use of Neutrons for the Investigation of Condensed Matter* (Clarendon Press, Oxford, England, United Kingdom, 1971), pp. xxiii, 599.

[67] S. Klotz, T. Hansen, E. Lelièvre-Berna, L. Amand, J. Maurice, C. Payre, E. Lelièvre-Berna, and P. Willendrup, Advances in the use of Paris-Edinburgh presses for high pressure neutron scattering, J. Neutron Res. **21**, 117 (2019).

[68] D. J. Carter and A. L. Rohl, Benchmarking calculated lattice parameters and energies of molecular crystals using van der Waals density functionals, J. Chem. Theory Comput. **10**, 3423 (2014).

[69] M. Obata, M. Nakamura, I. Hamada, and T. Oda, Improving the description of nonmagnetic and magnetic molecular crystals via the van der Waals density functional, J. Phys. Soc. Jpn. **84**, 024715 (2015).

[70] S. F. Yuk, I. Sargin, N. Meyer, J. T. Krogel, S. P. Beckman, and V. R. Cooper, Putting error bars on density functional theory, Sci. Rep. **14**, 20219 (2024).